A K_u-Band CMOS FMCW Radar Transceiver for Snowpack Remote Sensing

Yanghyo Kim, *Senior Member, IEEE*, Theodore J. Reck, *Senior Member, IEEE*,
Maria Alonso-delPino, *Member, IEEE*, Thomas H. Painter, Hans-Peter Marshall, Edward H. Bair,
Jeff Dozier, *Life Senior Member, IEEE*, Goutam Chattopadhyay, *Fellow, IEEE*,
Kuo-Nan Liou, Mau-Chung Frank Chang, *Life Fellow, IEEE*,
and Adrian Tang, *Senior Member, IEEE*

Abstract— This paper presents a K_u-band (14–16 GHz) CMOS frequency-modulated continuous-wave (FMCW) radar transceiver developed to measure dry-snow depth for water management purposes and to aid in retrieval of snow water equivalent. An on-chip direct digital frequency synthesizer and digital-to-analog converter digitally generates a chirping waveform which then drives a ring oscillator-based K_u-Band phase-locked loop to provide the final K_u-band FMCW signal. Employing a ring oscillator as opposed to a tuned inductor-based oscillator (LC-VCO) allows the radar to achieve wide chirp bandwidth resulting in a higher axial resolution (7.5 cm), which is needed to accurately quantify the snowpack profile. The demonstrated radar chip is fabricated in a 65-nm CMOS process. The chip consumes 252.4 mW of power under 1.1-V supply, making its payload requirements suitable for observations from a small unmanned aerial vehicle.

Index Terms— CMOS, frequency-modulated continuous-wave (FMCW), phase-locked loop (PLL), range correlation, ring oscillator, snow depth measurement.

I. INTRODUCTION

WHILE climate change has influenced a large portion of the earth in terms of temperature, sea water level, and precipitation, some of the most dramatic effects have appeared in the snowpack reduction and the subsequent water

Y. Kim and A. Tang are with the Jet Propulsion Laboratory, Pasadena, CA 91109 USA, and also with the Department of Electrical Engineering, University of California at Los Angeles, Los Angeles, CA 90095 USA (e-mail: rod.kim@jpl.nasa.gov; adrian.j.tang@jpl.nasa.gov).

T. J. Reck, M. Alonso-delPino, T. H. Painter, and G. Chattopadhyay are with Jet Propulsion Laboratory, Pasadena, CA 91109 USA (e-mail: theodore.reck@jpl.nasa.gov; maria.alonso@jpl.nasa.gov; thomas.painter@jpl.nasa.gov; goutam.chattopadhyay@jpl.nasa.gov).

H.-P. Marshall is with the Department of Geosciences, Boise State University, ID 83725 USA (e-mail: hpmarshall@boisestate.edu).

E. H. Bair and J. Dozier are with the Bren School of Environmental Science and Management, University of California at Santa Barbara, Santa Barbara, CA 93106 USA (e-mail: nbair@eri.ucsb.edu; dozier@bren.ucsb.edu).

K.-N. Liou is with the Department of Atmospheric and Oceanic Sciences, University of California at Los Angeles, Los Angeles, CA 90095 USA (e-mail: knliou@atmos.ucla.edu).

M.-C. F. Chang is with the Department of Electrical Engineering, University of California at Los Angeles, Los Angeles, CA 90095 USA (e-mail: mfchang@ee.ucla.edu).

Color versions of one or more of the figures in this paper are available online at http://ieeexplore.ieee.org.

Digital Object Identifier 10.1109/TMTT.2018.2799866

Fig. 1. (a) NASA worldview snow cover photograph taken in 2014. (b) Photograph taken in 2015.

availability within the state of California. The snowpack in the Sierra Nevada, which provides 60% of the water supply for California [1], has recorded an annual reduction of at least 20%–30% over the last five years (2011–2016), and as a result, the majority of the southwestern U.S. had suffered prolonged Stage 4 (extraordinary level) drought conditions during this period. As an example of these extraordinary climatic effects, Fig. 1(a) and (b) show photographs (NASA worldview) taken in 2014 and 2015, which display diminished snow cover across the entire Sierra Nevada. As snowpack retreats, the available water from snowmelt is limited and more vigorous water resources management is required to ensure that water demands are met throughout the state. The key to this planning exercise is accurately estimating the water content or snow water equivalent (SWE) available from snowpack, preferably weeks or months before the melting process occurs.

Three major snow properties influence the water content of a frozen snowpack: snow cover, snow depth, and snow density. Currently, each parameter is measured independently to produce a robust SWE estimate. The snow cover represents the area covered by snow, which can be either flat or on a 3-D terrain. Optical/IR remote sensing from space/airborne platforms can detect snow cover over the surface accurately, but is unable to penetrate into snow layer. The snow depth is the total depth of snow at each point within the snow cover, and the snow density is the measure of how packed snow is. As shown in Table I, space-borne microwave sensors (active and passive) estimate the snow density within a 20% error, but provide poor snow depth estimates (40% error) because of their aperture limited spatial resolutions ($\sim$25 km) [2]. Beyond spatial footprints, empirical measurements described in [3] indicate that snow depth resolutions better than 10 cm are required for a robust SWE estimation.

TABLE I
SUMMARY OF EXISTING SWE ESTIMATE TECHNIQUE

	Microwave	IR	Optical
Snow Cover Estimate	Reasonable	Excellent	Excellent
Snow Depth Estimate	40 % Error	N/A	N/A
Attainable Resolution	25 km	100 m	10 m
Snow Density Estimate	>20 % Error	N/A	N/A

This paper focuses on the development of a K_u-band CMOS frequency-modulated continuous-wave (FMCW) radar to improve depth measurements of dry snow toward producing more precise SWE estimates. In this approach, a radar is flown on a small unmanned aerial vehicle (UAV) at low altitudes in the range of 100 m to overcome the aperture limited spatial resolution of space-borne microwave snow sensing. A 100 m is chosen to accommodate the height of the tall Giant Sequoia trees in Sierra Nevada forests. Considering the aperture limited spatial resolution

$$\Delta x \cong \frac{\lambda}{d} R \qquad (1)$$

where λ is the wavelength (2 cm at 15 GHz), d is the antenna diameter (assumed to be 30 cm based on the UAV size), and R is the target distance, a spatial resolution of 6 m can be achieved from a 100-m altitude, far better than the 25 km of space-borne instrumentation. As mentioned, an axial resolution of better than 10 cm is demanded, and since the resolution is expressed as

$$\Delta R = \frac{c}{2B} \qquad (2)$$

where c is the speed of light, and B is the chirp bandwidth, a chirp bandwidth of at least 1.5 GHz is required. As a small UAV is considered, a fully integrated CMOS integrated circuit is highly desirable to accommodate the limited payload and power availability. Considering operation frequencies and signal-to-noise ratio (SNR) involved in snow sensing (discussed in the next section), the radar's required fractional bandwidth will be quite high (in excess of 10%), implying waveform generations will be challenging. Using a traditional CMOS radar approach with an arbitrary waveform generator (AWG) on a CMOS chip demands wideband (3 GS/s in our case) digital-to-analog converters (DACs) and an excessive memory length for reasonable chirp times of 100–1000 μs (well beyond 64 K points). CMOS LC-voltage-controlled oscillator (LC-VCO)-based approaches are also inadequate as they report on the order of 5% continuous tuning bandwidth at best limited by the poor quality factor of on-chip varactors [4], [5].

As an alternative the proposed architecture employs a direct phase-locked loop (PLL)-based chirp generation [5], equipped with a ring-VCO to achieve a 2-GHz chirp bandwidth, equivalently 7.5-cm axial resolution [6]. While ring-VCOs are notorious for poor phase noise, the relatively short distance operation (<100 m) allows to exploit the range correlation effect [7] where radar's phase noise is significantly canceled because of the sharing of the transmit and receive local oscillator (LO).

II. ELECTRICAL PROPERTIES OF SNOW

This section explains electrical properties of snow to understand the feasibility of penetration at K_u-band based on previously performed experimental research [8]–[12]. Dry snow consists of air and ice, whereas wet snow contains liquid water content as well. The goal of this section is to provide information on the real and imaginary part of dry-snow's dielectric constant such that a loss factor can be calculated. To begin with, the dielectric constant of air is 1 without loss factor. Ice, according to [8], offers a dielectric constant with a real part of 3.17, and an imaginary part that is a function of frequency and temperature. The Tinga–Voss–Blossey (TVB) formulas suggest that the effective dielectric constant of mixture materials depends on each individual substance and its volume fraction [9]. Therefore, one can infer that the real part of dry snow depends only on snow density, whereas the imaginary part varies over snow density, frequency and temperature. The above observation has been experimentally validated in [10] and [11]. For example, the empirically modeled real part of dry snow is expressed as

$$\varepsilon' = (1 + 0.508\rho_s)^3 \qquad (3)$$

where ρ_s is the snow density, and it agrees with the TVB formulas up to 37 GHz. As shown in Fig. 2(a), the real part ranges from 1.4 to 2.4 for snow densities of 0.2 to 0.6 g/cm^3. For the imaginary part, the empirical model is expressed as

$$\varepsilon'' = \frac{0.34V_i\varepsilon_i''}{(1 - 0.417V_i)^2} \qquad (4)$$

where V_i is the ratio of ice density and snow density, and ε_i'' is the imaginary part of ice dielectric constant. The imaginary part of dry snow can be plotted as shown in Fig. 2(b). In general, as the frequency and density increases, the loss factor also increases. Combining the real and imaginary values, the absorption coefficient can be determined

$$\alpha = \omega \left\{ \frac{\mu\epsilon'}{2} \left[\sqrt{1 + \left(\frac{\epsilon''}{\epsilon'}\right)^2} - 1 \right] \right\}^{\frac{1}{2}} \qquad (5)$$

where ω is the angular frequency and μ is the magnetic permeability. Dry snow exhibits no magnetization, which means that the permeability is the same as the air. Based on (5), the absorption coefficient is plotted in Fig. 2(c). In the case of the dry snow depth of 8–10 m, a round-trip absorption loss would be less than 10 dB at 15 GHz.

As the frequency of operation increases beyond the 15-GHz regime, an intergrain scattering mechanism starts to dominate over the bulk absorption (Mie regime). For a typical snow particle with a diameter of 0.2–1.5 mm, electromagnetic theories suggest that the Rayleigh-scattering regime will occur below 15 GHz so that absorption effects dominate, while above 15 GHz, the Mie-scattering regime must be considered where the beam scattering is dominated by grain size [12]. Employing available data sets and model at these wavelengths [11], [12], extinction coefficients (absorption + scattering) over various grain size conditions are illustrated in Fig. 2(d). Note that the loss could reach 1000 dB/m at mm-wave frequencies for the
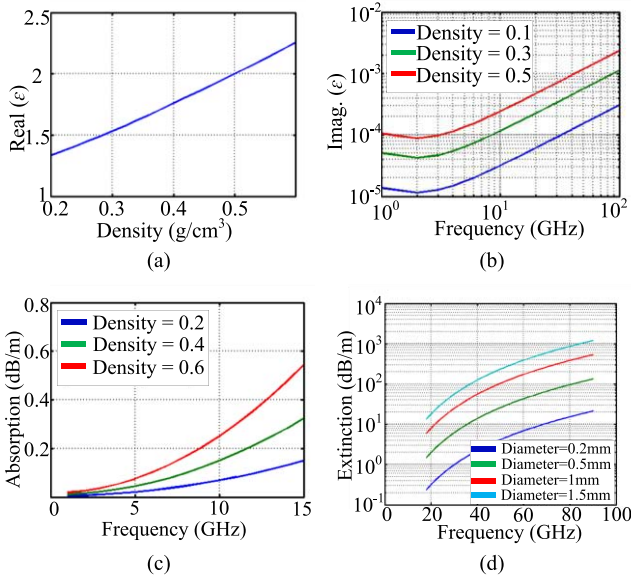
Fig. 2. (a) Real part of dry-snow's dielectric constant versus density. (b) Imaginary part of dry-snow's dielectric constant versus frequency. (c) Absorption coefficient of dry snow versus frequency. (d) Extinction coefficient of dry snow versus frequency.

TABLE II
RADAR SYSTEM ASSUMPTIONS

Parameters	Values
Antenna Size (A)	30 cm (aircraft payload)
Transmit Power (Pt)	0.5 W (available hardware)
RX Noise Figure (NF)	7 dB
Bandwidth (B)	2 GHz (from resolution)

TABLE III
SCENARIO ASSUMPTIONS

Parameters	Values
Range/Altitude (R)	100 m (avoid trees)
Scatter Coefficient (σ)	-12 dB (worst case)
Temperature (T)	250 K (worst case)
Snow Losses (S)	10 dB (from study)

snow diameter of 1.5 mm. Given these absorption/extinction coefficients and recognizing the need to penetrate historical record snow depths (10 m in the Sierra), while at the same time considering the aperture limited resolution (target of 6-m resolution with a 30-cm antenna) from various altitudes at which the radar will conduct the remote sensing operation, 15 GHz (mid-K_u-band) is selected as an optimal frequency for remotely sensing snowpack properties, providing a compromise between SNR, aperture limited spatial resolution, and snowpack penetration.

III. SNR AND DYNAMIC RANGE ESTIMATION

Using the loss factor of dry snow and scenario assumptions (Tables II and III), the SNR and dynamic range requirements can be established for the snow sensing radar. The CMOS radar chip drives a commercially available (Mini Circuits

TABLE IV
SNR ESTIMATION AT THE ALTITUDE OF 100 m

S (dB)	S (Linear)	σ (Linear)	T (K)	Pt (W)	A (m)	B (GHz)	NF (Linear)	SNR (dB)
-5	0.3	0.1	250	0.5	0.3	2	2	31.5
-10	0.1	0.1	250	0.5	0.3	2	2	26.5
-15	0.5	0.1	250	0.5	0.3	2	2	21.5
-20	0.24	0.1	250	0.5	0.3	2	2	16.5
-25	0.55	0.1	250	0.5	0.3	2	2	11.5

TABLE V
DYNAMIC RANGE ESTIMATION

Parameters	Best Case	Worst Case	Variation
Snow Absorption	0 dB	-20 dB	20 dB
Scatter Coefficient	-1 dB	-12 dB	11 dB
Altitude of UAV	25 m	200 m	12 dB
Minimum SNR			10 dB
Dynamic Range			53 dB

ZVA 183+) external power amplifier (PA), which delivers 0.5 W of output power. In terms of measurement scenario, the ground scattering coefficient is assumed to be -12 dB in the worst case based on empirical data [13], and the worst-case environmental temperature experienced in the mountain area is estimated at 250 K. Based on these assumptions, an SNR model from [14] is employed as

$$\text{SNR} = \frac{\sigma \cdot P_t \cdot A \cdot S}{4\pi \cdot k \cdot T \cdot B \cdot NF \cdot R^2} \qquad (6)$$

where σ is the scattering coefficient, P_t is the transmit power, A is the antenna size, S is the snow loss from Section II, k is the Boltzmann's constant, B is the bandwidth, and R is the altitude. As shown in Table IV, even when dry snow undergoes a 25-dB loss, the radar system exhibits an 11.5-dB SNR when observing from 100 m.

Of course, the scenario assumptions will vary over different environments. For instance, propagating waves may experience different loss through dry snow depending on the conditions of snow density, temperature, and grain size. By repeating the loss factor estimates at extreme conditions for each, variations of loss factor across all conditions are estimated in the range of 20 dB. The scattering coefficients of ground also vary depending on surface roughness, terrain slope, and polarization (possibly 10 dB better than worst-case assumptions). Finally, the UAV could fly either at higher or lower altitudes depending on the height of trees. Reserving another 10 dB of minimum SNR for the situations where the radar may encounter, the required dynamic range of the snow radar system is calculated as 53 dB as shown in Table V. The estimation translates to an effective number of bits of 8.5 when choosing data converters.

IV. K_u-BAND FMCW RADAR DESIGN

As mentioned in the introduction, the demonstrated radar system targets a 7.5-cm axial resolution based on SWE estimate requirements, which results in a chirp bandwidth of
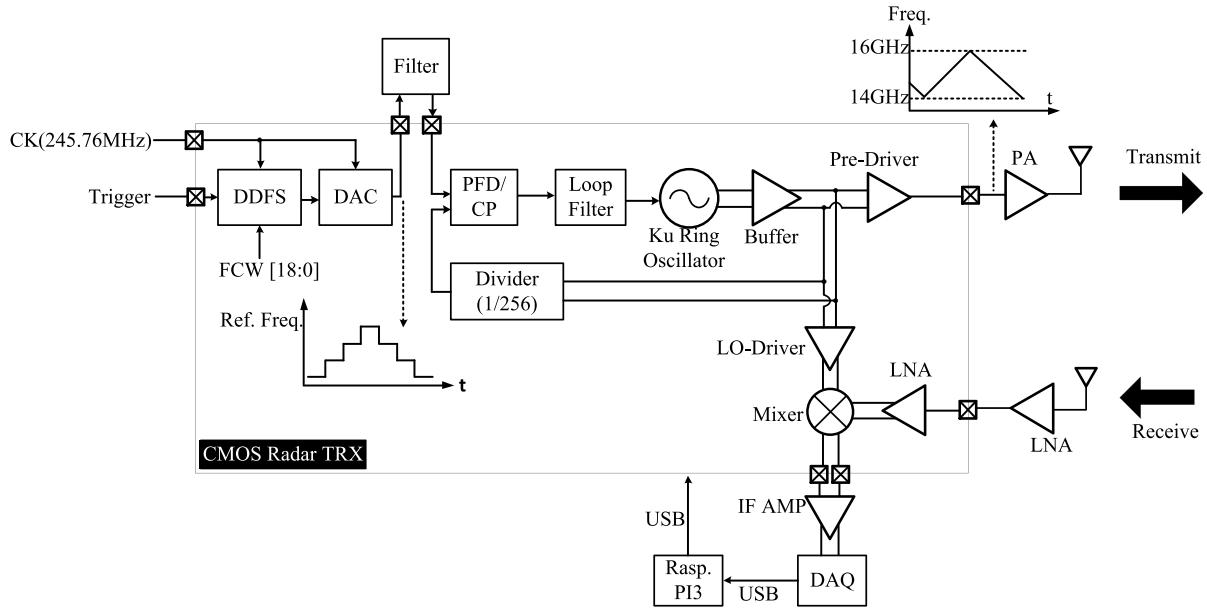
Fig. 3. Radar system block diagram.

2 GHz (13% fractional bandwidth at 15 GHz). To achieve a compact transceiver architecture while supporting such a wide chirp bandwidth, a direct PLL-based chirp generation [5] equipped with a ring-VCO and driven by a direct digital frequency synthesizer (DDFS) is adopted [6], [15]. The PLL accepts a low frequency reference chirp from the DDFS, synthesizes, and interpolates to turn a discrete frequency staircase into a smooth frequency ramp. The overall system block diagram is shown in Fig. 3. The CMOS radar transceiver consists of a reference chirp generator, which is a combination of DDFS and DAC, PLL, high-speed buffer, transmitter (TX) predriver, receiver (RX) low-noise amplifier (LNA), and down-conversion mixer, all integrated within a single chip.

A. Reference Chirp Generator and Radar Specification

The digital implementation of 19-bit precision DDFS, which consists of phase accumulator and sine lookup table (sine ROM), is shown in Fig. 4(a) [16]. The phase accumulator tracks output phases, and the sine ROM converts current phase information into a 10-bit voltage value, which is then sent to a 10-bit DAC. In the phase accumulator, the 20-bit register represents an output signal's single period using values from 0 to $2^{20} - 1$. At each clock cycle, a frequency control word (FCW) is added to the accumulator to advance its phase. Therefore, a frequency ramp of discrete frequency steps (staircase) can be created by synchronously counting the FCW. This action of frequency sweep (up and down) is fully synchronized via an external trigger signal as shown in Fig. 4(b). At the rising edge of trigger, the frequency increases until its predetermined stop-FCW and waits until the trigger falls. At the falling edge of trigger, the frequency decreases until its start-FCW. The main advantage of this synchronous operation is that it avoids distortion and frequency errors at the turn-around regions by capturing only the linear portions of the chirp. For the demonstrated FMCW system, an externally provided 245.76-MHz
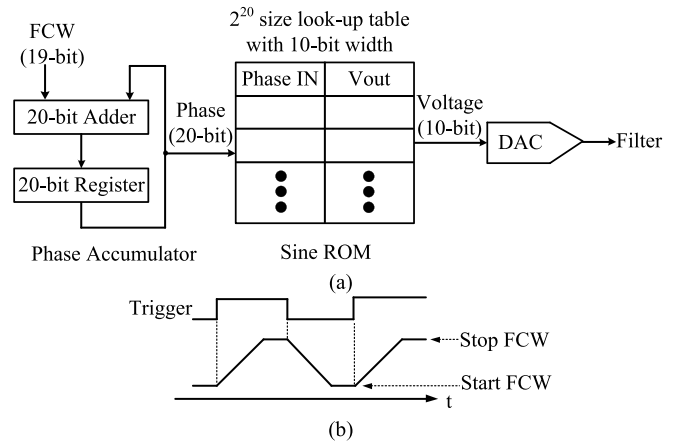

Fig. 4. (a) DDFS implementation. (b) Synchronized frequency sweep up and down operation with trigger.

crystal clocks the combination of DDFS/DAC and produces the reference FMCW chirp signal from 54.6875 to 62.5 MHz considering the PLL's operation range of 14–16 GHz and its fixed division ratio of 256. With the 245.76-MHz clock frequency and 19-bit FCW, each frequency step is 234.375 Hz during the chirp (Nyquist Rate/2^{19}).

By implementing such a high-resolution and high-speed on-chip DDFS, the frequency step accuracy is improved more than 24 times compared to the previous work presented in [5], ensuring that chirp nonlinearity is minimal. Considering the total FCW code range from 233333 (54.6875 MHz/234.375 Hz) to 266667 (62.5 MHz/234.375 Hz) corresponding to the PLL's chirp bandwidth and the clock period of 0.004 μs, the chirp time (radar integration time) is derived at 135.64 μs [(266667 − 233333) × 0.0004 μs], which is short enough to acquire samples from an aircraft without motion-induced blurs.

RF Chirp Parameter	
Chirp Bandwidth (GHz)	2
Range Resolution (cm)	7.5
Frequency Low (GHz)	14
Frequency High (GHz)	16
PLL Division Ratio	256
Reference Chirp Parameter	
Reference Low (MHz)	54.6875
Reference High (MHz)	62.5
DDFS Parameter	
Clock Frequency (MHz)	245.76
Clock Period (μs)	0.004
Accumulator Bits	19
Step Size (Hz)	234.375
Reference BW (Codes)	33334
Chirp Time (μs)	135.64
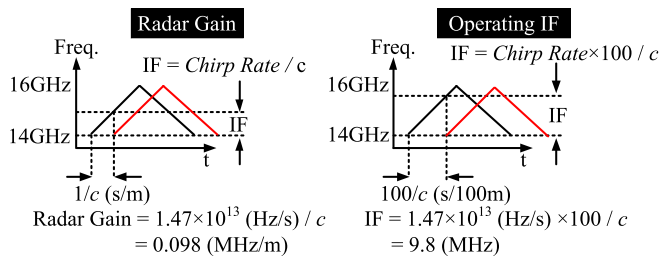
Fig. 5. Radar performance calculation.

The above calculation of radar specification is summarized in Table VI. The current-steering-based high-speed DAC is designed with a 10-bit physical resolution based on the design described in [17]. The analog reference chirp output is fed into an external anti-aliasing filter before being provided to the phase/frequency detector (PFD) of the on-chip PLL.

To quantify the radar performance, using the chirp time and chirp bandwidth, the chirp rate is calculated as 1.47×10^{13} Hz/s (2 GHz/136.64 μs). Then, the radar gain is calculated as 0.098 MHz/m (Chirp Rate/c) as shown in Fig. 5. This means that every 1 m of target range advance is equivalent to a 0.098-MHz offset at the intermediate frequency (IF) output. Since the expected altitude of observing aircraft or UAV is 100 m, the final returned IF from snowpack should occupy 9–10 MHz regions. The maximum IF frequency of interest determines the sampling speed required by an analog-to-digital converter. In this case, A 20 MS/s is the minimum sampling speed to meet the Nyquist criteria.

B. RF-Signal Path

The detailed schematic of RF-signal path is shown in Fig. 6. In the PLL path, a four-stage ring oscillator is implemented to provide both in-phase (I) and quadrature-phase (Q) carrier signals for a single-sideband processing when necessary. Although the ring-VCO exhibits much higher phase noise than an LC-VCO, the demonstrated FMCW radar system reduces the amount of phase noise after down-conversion at the IF as

the transmit and receive LO are shared. This effect is referred to as range correlation, and is beneficial when targets are within short range. More details on range correlation will be explained in the following section. As shown in Fig. 7(a), each ring cell consists of a differential input pair and cross-coupled pMOS load, and the extra pMOS device tunes the frequency with a varying amount of current. As described in Fig. 7(b), the designed ring-VCO runs from 17.2 to 13.2 GHz over 0.2-V control voltage range. It results in −20 GHz/V VCO gain (K_{VCO}). For comparative purposes, an inductor-based K_u-band VCO is designed using the same CMOS technology in Fig. 7(c). As simulated in Fig. 7(d), the LC-VCO fails to cover the required 2-GHz bandwidth continuously.

The ring-VCO simultaneously drives a predriver for the TX path, an LO driver for the down-conversion path, and a current-mode logic (CML)-based divider for the PLL path. The above loading conditions not only lower the operating frequency, but also create a risk the VCO will not startup. Therefore, at the I and Q port from the ring-VCO, five stages of resistor-loaded high-speed differential amplifiers are inserted as a buffer. In the PLL path, three stages of CML divider initially divide the 14–16-GHz chirp signal down to the 1.75–2-GHz frequency. The CML divider's schematic is shown in Fig. 8(a), and its minimum required differential input swing over the operating frequency is simulated in Fig. 8(b). The simulation result indicates that the buffer needs to provide at least 40-mV swing differentially to the CML divider. After CML divider stages, five stages of static divider are designed using standard digital gates to further divide down to the 54.6875–62.5-MHz reference frequency. The PFD compares the divider's output signal and reference chirp signal coming from the DDFS/DAC. The PFD and charge pump are designed as a pseudodifferential structure [18].

In the TX path, the predriver is designed with a transformer-coupled common-source amplifier to deliver 2–5-dBm output power as well as convert differential signals to single-ended signals for the external PA to accept. In the down-conversion path, the LO driver is also designed with a transformer-coupled common-source amplifier, providing sufficient signal swing to completely switch the down-conversion mixer's commutation devices. In the RX path, a one-stage on-chip LNA converts single-ended signals to differential signals and provides a 10–14-dB gain with a noise figure performance of 7 dB (simulated in Fig. 6). The on-chip Gilbert cell mixer outputs I and Q IF signals for further fast Fourier transform (FFT) processing in an oscilloscope or data acquisition (DAQ) system.

To facilitate better understanding of the above operations, a transient simulation is performed, including ring-VCO, buffer, TX predriver, LO buffer, and divider with the chain in an open loop configuration as shown in Fig. 9. The ring-VCO's control voltage is manually swept from 0.37 to 0.27 V (the same region occupied by the chirp). As shown in the plot, after the buffer stage, the differential swing (480 mV) is reduced by almost half compared to the ring-VCO's output. In the TX path, the predriver amplifies and delivers necessary output power to the 50-Ω load presented by the external PA. In the down-conversion path, the LO driver amplifies and
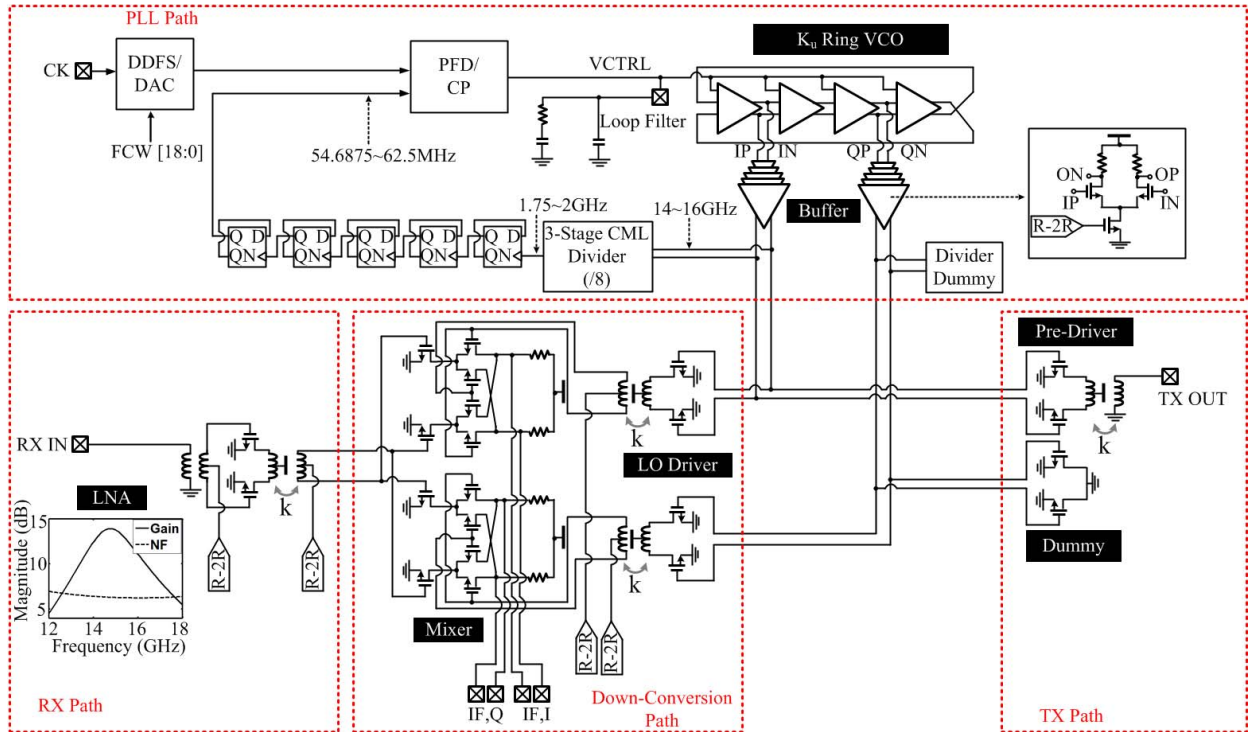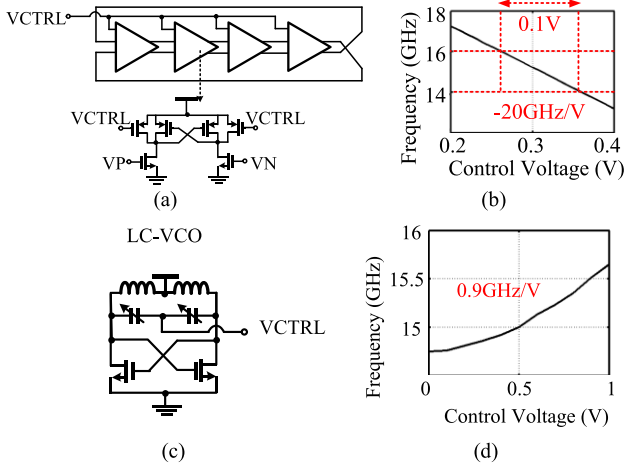
Fig. 6. Detailed schematic of RF-signal path.

Fig. 7. (a) Schematic of ring VCO's unit cell. (b) Ring-VCO's frequency versus control voltage. (c) Schematic of *LC*-VCO for bandwidth comparison purpose. (d) *LC*-VCO's frequency versus control voltage.

Fig. 8. (a) Schematic of CML latch and divider. (b) Minimum required swing at the divider input versus frequency.

TABLE VII
PLL PARAMETERS

PLL Parameter	
Division Ratio	256
CP Current (mA)	0.8
KVCO (GHz/V)	20
Loop Bandwidth (MHz)	1

provides enough swing for the down-conversion mixer. In the PLL path, the CML divider divides 14–16-GHz chirp signal successfully using 480-mV swing at its input without extra amplifier stages between the buffer and divider stages.

C. PLL Parameters and System Simulation

To understand the frequency chirp behavior, the PLL parameters and loop behavior are studied in Table VII and Fig. 10(a) and (b). The loop bandwidth of the PLL is selected with the following criteria:
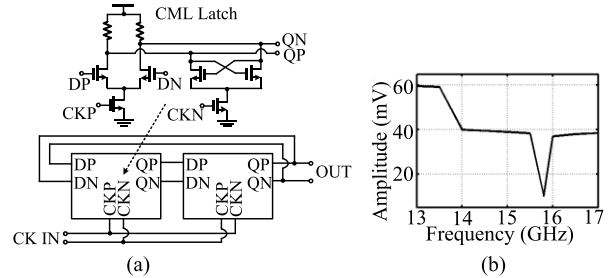
$$\frac{1}{\text{Chirp Time}} < \text{PLL Bandwidth} < \text{Clock Speed}. \qquad (7)$$

From the radar specification in Table VI, the PLL bandwidth falls between 1.9 kHz (1/Chirp Time) and 245.76 MHz (clock speed). Therefore, the target loop bandwidth is set at 1 MHz, which is approximately 3 orders of magnitude apart from each frequency boundary. Using K_{VCO} from Fig. 7(b), PLL charge pump current, and division ratio, the loop filter values are
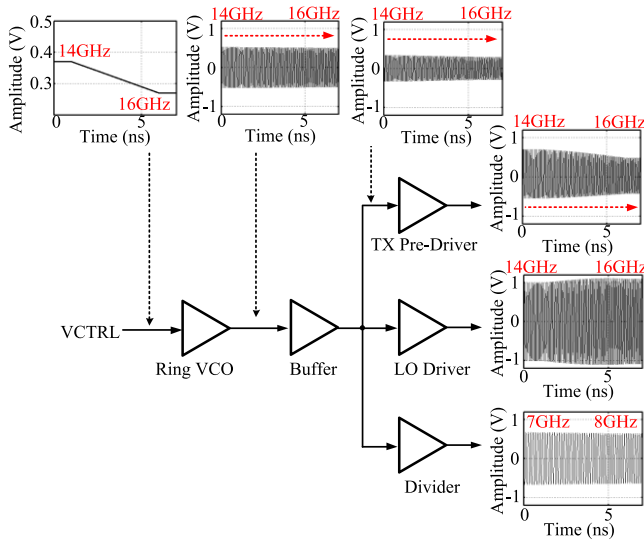
Fig. 9.   14–16-GHz chirp transient simulation for ring-VCO, buffer, TX predriver, LO buffer, and divider.
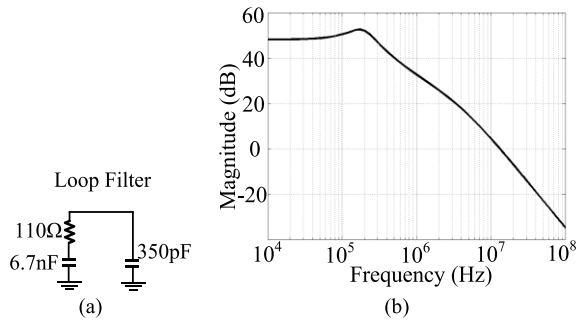

Fig. 10.   (a) Loop filter values. (b) PLL transfer function.

selected as shown in Fig. 10(a). The corresponding closed-loop transfer function of type-II PLL is plotted in Fig. 10(b).

In order to demonstrate the filter values are suitable for frequency synthesis and interpolation, the following system simulation is performed using MATLAB software in Fig. 11. Note that the PLL analysis relies on input and output phases in frequency domain, which means that once the input phase is known, the output phase can be calculated by the multiplication of PLL transfer function and input phase. In the case of the demonstrated FMCW radar, the input to the PLL is given with frequency steps in time domain, as shown in Fig. 11(a). The frequency chirp becomes a phase chirp in time domain after integration in Fig. 11(b), and then, the FFT converts the phase signal in time domain to a frequency-domain signal shown in Fig. 11(c), which is the proper input to the PLL transfer function. The transfer function in Fig. 11(d) is the linear scale version of the transfer function in Fig. 10(c). At steady-state, the closed-loop gain is 256, which is the division ratio of the PLL. After multiplication of the input phase and the PLL transfer function, the output phase in the frequency domain is plotted in Fig. 11(e). An inverse FFT (iFFT) takes the phase signal back to the time domain in Fig. 11(f), and finally, the synthesized (frequency multiplication) and

interpolated (smooth ramp) output frequency chirp is plotted after derivative operation in Fig. 11(g).

D. Range Correlation

The ring-VCO's phase noise becomes problematic when there are secondary scatters (often called clutter) around targets of interests. In the case of snow depth measurement, there will be mainly two returned signals: one from snow cover, and the other from the ground. Since both snow cover and ground information is necessary to retrieve the snow depth (frequency difference at IF divided by the radar gain), either snow cover or ground can act as an unwanted clutter. Applying the scenario assumptions and radar specification, the frequency difference between snow and ground is expected to be within 1 MHz, as the radar gain is 0.098 MHz/m and expected snow depths are under 10 m (0.098 MHz × 10 m = 0.98 MHz).

From a phase noise perspective, it is more critical when the depth of snow is shallow rather than deep, because the close-in phase noise at 100 or 200 kHz could be as high as −50 dBc/Hz. To overcome the high phase noise of ring-VCO, the demonstrated radar exploits the well-known range correlation effect [7], where the phase noise of radar LO is partially canceled when it is used for both transmission and RX down-conversion. As the reflected signal from a target is a delayed copy of the TX LO, and the same LO is used for down-conversion, the phase noise of these signals is all correlated. The degree of phase noise correlation is limited only by the difference in time (determined by the round-trip delay of the target path). The shorter the distance (and delay) to the target, the closer the correlation between the two signals at the down-converter and the better the cancellation. This effect can be modeled as an effective filter applied to the power spectral density of the LO phase noise [7]

$$S(f) = 4\sin^2\frac{2\pi R f}{c} \tag{8}$$

where R is the target distance, and f is the frequency at IF. The above filtering effect is demonstrated using simulated phase noise profiles from the ring-VCO and LC-VCO (designed in Fig. 7) when the operating frequency is 15 GHz, as shown in Fig. 12(a). As expected, the LC-VCO's phase noise performance is superior than that of the ring-VCO by more than 30 dB. The effect of PLL transfer function to the phase noise is not considered in this paper. Based on (8), the noise shaping functions of various target distances (1, 10, and 100 m) are plotted in Fig. 12(b). Note how the range correlation reduces the amount of phase noise, especially when the target distance is small. Even at 100 m, the phase noise cancellation at frequency offsets up to 200 kHz remains considerable. The effective phase noise profiles at the RX IF with range correlation considered are plotted in Fig. 12(c) and (d). The noise cancellation is apparent for 1- and 10-m cases for both the ring-/LC-VCO. For 100-m ranges, the range correlation contributes reducing the phase noise below 200 kHz; beyond 200 kHz, the natural roll-off of phase noise becomes sufficient not to interfere with the dynamic range of radar, approximately 53 dB as listed in Table V. Note that although the LC-VCO appears preferable for phase noise performance,
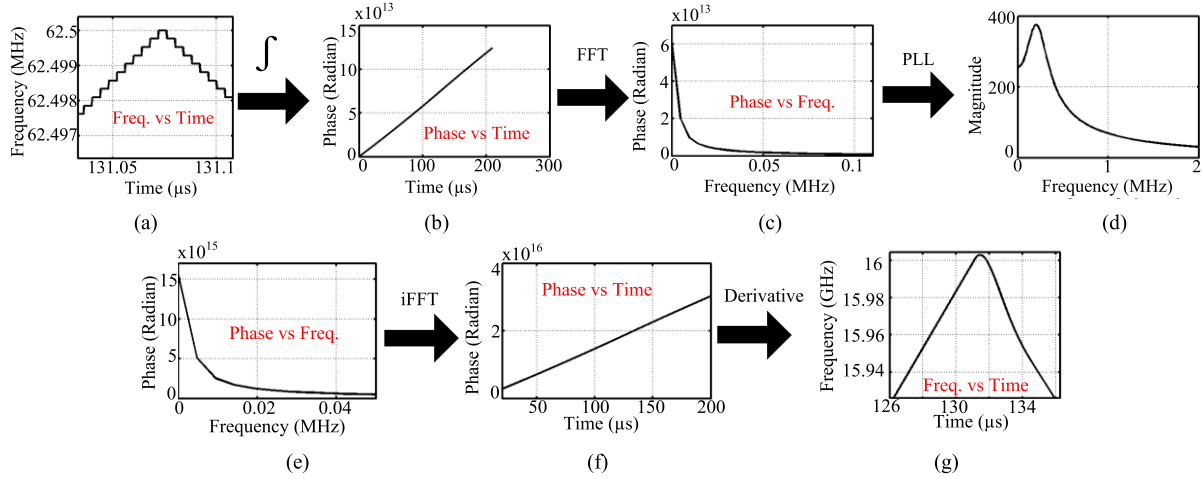
Fig. 11. PLL system simulation. (a) Reference chirp with frequency step. (b) Reference phase after integration in time domain. (c) Reference phase in frequency domain after FFT. (d) Reference input phase passes through PLL transfer function and generates output phase. (e) PLL output phase in frequency domain. (f) PLL output phase in time domain after inverse FFT. (g) Synthesized and interpolated final frequency output in time domain after derivative.
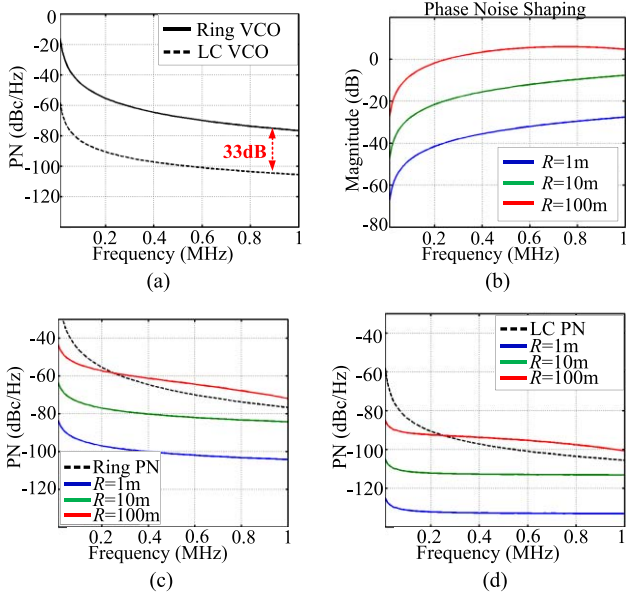

Fig. 12. (a) Simulated phase noise of ring oscillator when carrier frequency is 15 GHz. (b) Noise shaping function over various target distance. (c) Ring VCO's filtered phase noise profile at IF. (d) *LC*-VCO's filtered phase noise profile at IF.

it fails to meet bandwidth requirements for snow sensing as discussed in Sections II and III.

V. CMOS FABRICATION AND MEASUREMENT

A. CMOS Fabrication and Assembly

The radar transceiver is designed and fabricated in a 65-nm CMOS process with the die photograph shown in Fig. 13(a). The radar electronics module is designed to achieve a compact and portable package, and eventually suitable to deploy for conducting field measurements. The assembly block diagram is shown in Fig. 13(b), and the assembled electronics module without antennas is shown in Fig. 13(c). Discrete components

including anti-aliasing filter and crystal are mounted on the PCB, and additionally, an external OPAMP is added at the output of CMOS IF port to provide an additional 25-dB IF gain.

To enable stand-alone operations of the instrument in remote areas, a Raspberry PI3 embedded system drives the radar module, requesting measurements at pre-programmed times and saving returned data on a USB storage device. For data recording purposes, a compact DAQ module from Bitscope is connected at the output of IF OPAMP. The Bitscope DAQ samples the IF signal at 20 MS/s with an 8-bit physical resolution (approximately 48 dB of dynamic range). The data are stored in time-domain format and the FFT is computed offline on a PC during measurement retrievals.

B. Laboratory Measurements

Standard K_u-band horn antennas are used for a lab demonstration and a time domain waveform of the frequency chirp is captured by measuring the control voltage of the PLL. As mentioned in Section IV-A, an interval of constant frequency exists at each endpoint of frequency ramp (dwell time between chirp triggers). The time-domain return signal is measured at the IF port when the radar points directly at the floor 1.6 m away, illustrating the IF content with a modest distortion between chirps. These two time-domain waveforms are recorded in Fig. 14(a). In addition, the TX output is connected directly to a spectrum analyzer to confirm the chirp frequency with the measurement shown in Fig 14(b). Note that the full 14–16-GHz bandwidth is uniformly occupied, indicating that the FMCW chirp is highly linear (as equal chirp time is spent at each frequency). The large glitches at endpoints are a result of the dwell time between each chirp. To further characterize the overall effect of chirp distortions from the nonlinearity of the DDFS steps and PLL chirp response on the overall radar system range resolution, a point scatterer target (small smooth metal object) is placed at a distance corresponding to 16 FFT range bin and recorded 100 radar
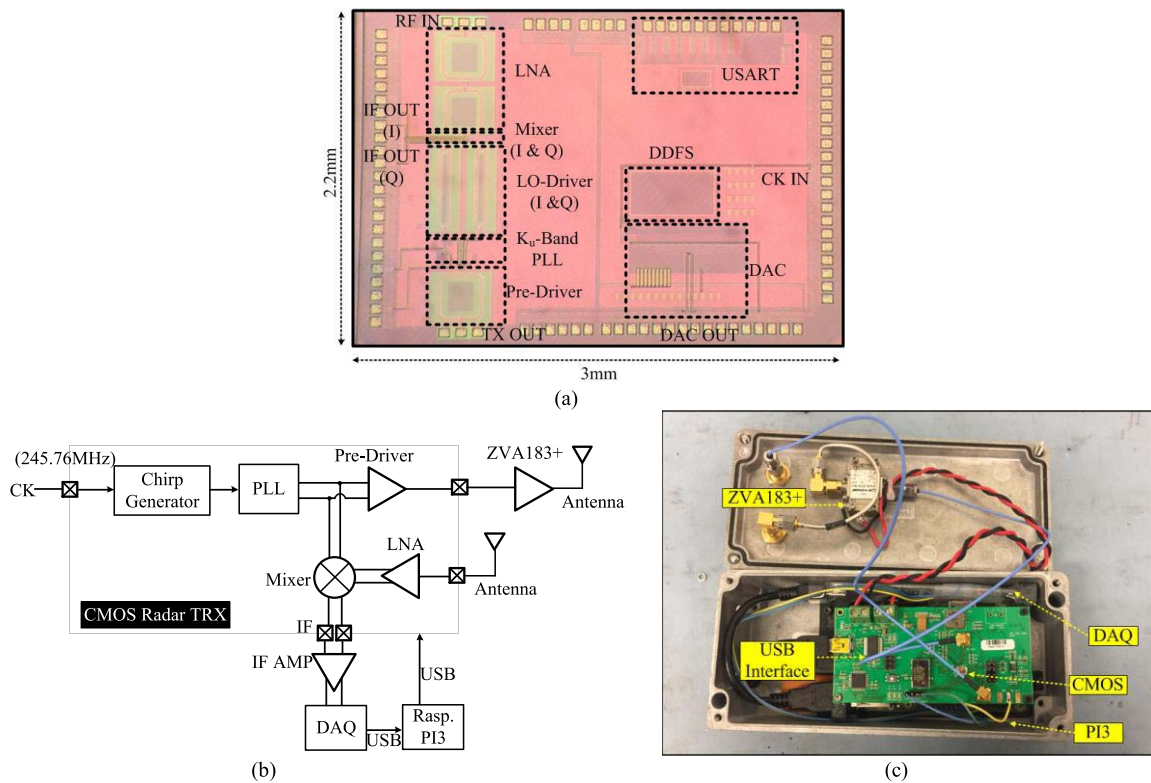
(a)

(b)

(c)

Fig. 13. (a) Fabricated CMOS chip in 65-nm process. The entire CMOS occupies 2.2- by 3-mm space. (b) Radar assembly block diagram with an external IF OPAMP, DAQ, and Raspberry PI3. (c) Assembled radar system module.
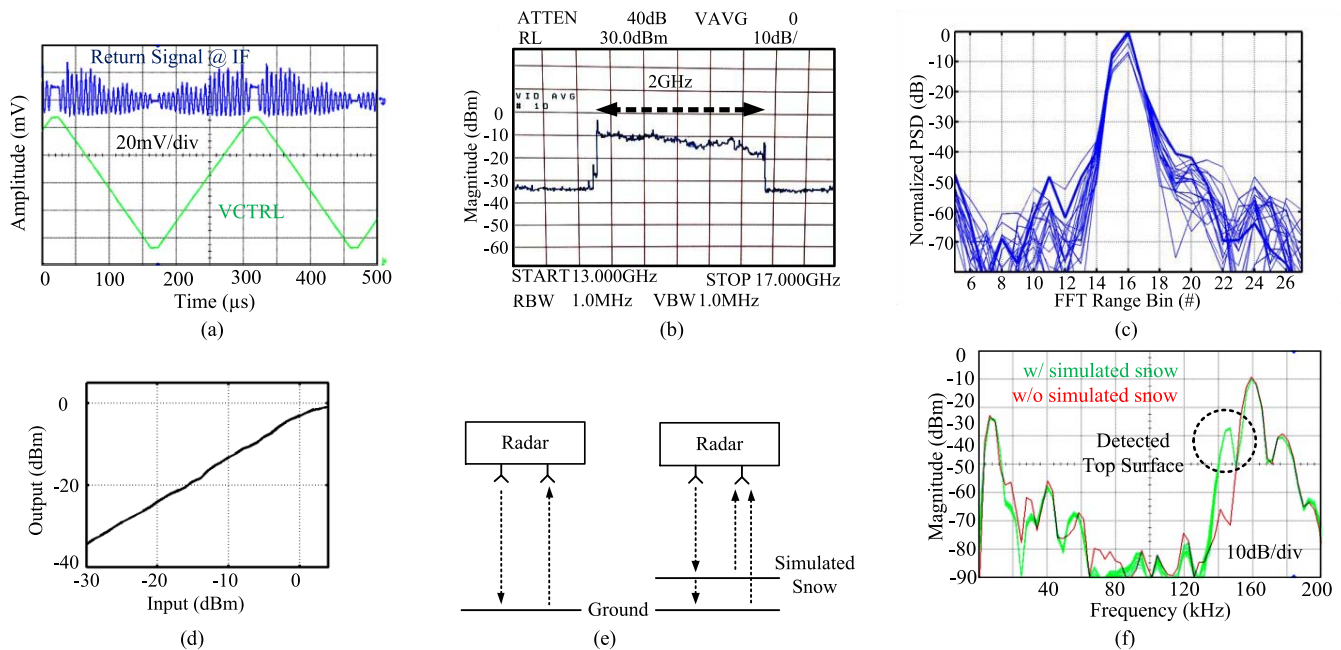

(a)

(b)

(c)

(d)

(e)

(f)

Fig. 14. (a) Measured frequency chirp at the control voltage test point and time-domain reference chirp signal. (b) Measured K_u-band FMCW spectrum with a 2-GHz chirp bandwidth. (c) Chirp distortion measurement using point scatterer. (d) Measured RX linearity. (e) Measurement diagram. (f) Measured spectrum with and without simulated snow target.

successive chirps then plotted the overlapping FFTs around the target as shown in Fig. 14(c). The measurement shows that the radar is indeed quite linear, with less than −30 dBc of leakage within two range bins of the target. Note that the sidelobes are not exactly symmetric due to the amplitude variation over the swept frequency bandwidth. The RX linearity is also measured in Fig. 14(c), indicating the RX starts to saturate at −2-dBm input power. To demonstrate the targeted measurement of

TABLE VIII
SUMMARY OF THE POWER CONSUMPTION

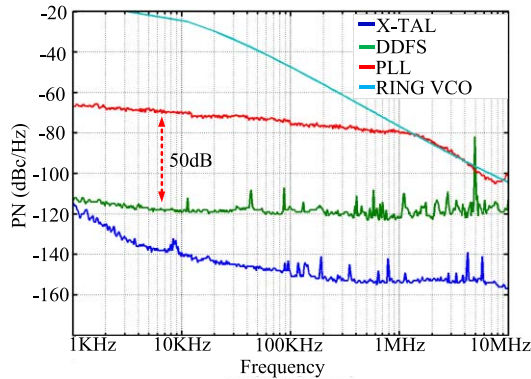| CMOS Power Summary	
VDD	1.1 V
PLL	92 mA
Pre-Driver	18 mA
LO-Driver	12 mA
LNA	15 mA
Mixer	7 mA
DAC	25 mA
DDFS	65 mA
Total	252.4 mW
External Component	
ZVA 183+	5.2 W

Fig. 15. Measured phase noise of 245.76-MHz crystal, 58.6-MHz reference signal from DDFS + DAC, 15-GHz frequency synthesizer output, and simulated phase noise of ring oscillator. The frequency chirp is turned OFF for the measurement by fixing the FCW at 2 50 000.

snowpack depth in a lab environment, a 10-cm (comparable to the radar resolution) box of Styrofoam pellets, which has similar dielectric properties to dry snow, is placed in the radar beam. The IF time-domain signal is captured, and the FFT is computed with and without the simulated snowpack present. Fig. 14(e) compares the two measurements showing the snowpack surface is clearly detected by the instrument. The summary of power consumption is shown in Table VIII. The CMOS chip consumes 252.4-mW power from a 1.1-V power supply, and the external PA (ZVA 183+) consumes 5.2 W (dominant power consumption in the system) from a 12-V power supply.

C. Phase Noise and Range Correlation Measurement

The phase noise of implemented radar system is measured to characterize the range correlation behavior. To establish reference data for a comparison before and after the range correlation, the phase noise of reference crystal (245.76 MHz), reference chirp generator (DDFS + DAC), and PLL are first measured using a signal source analyzer (E5052B), as shown in Fig. 15. The FCW code of the reference chirp generator is fixed at 2 50 000 to generate a continuous-wave signal, which is equivalent to 58.6 MHz. The measured phase noise of reference chirp generator reads −110 dBc/Hz across 10-MHz

bandwidth, which is limited by the quantization noise of the on-chip DAC. After frequency synthesis through the PLL, the TX generates 15-GHz continuous-wave signal. Based on a 256-frequency multiplication factor, the phase noise penalty from the reference phase noise is calculated as $20\log_{10}256 = 48.1$ dB. The measurement result agrees well with a mathematical prediction. The simulated phase noise of ring-VCO also agrees well with the measurement; the phase noise is dominated by the reference signal within the PLL bandwidth ($\sim$1 MHz), and the noise profile follows the ring-VCO beyond the loop bandwidth. The block diagram of phase noise measurement setup capturing the range correlation effect is shown in Fig. 16(a). Similar to the base phase noise measurement, the FCW of chirp generator is fixed at 2 50 000 to generate a 15-GHz continuous-wave signal. In order to emulate the delayed return signal, a 2-m coax cable is inserted between TX and RX signal path. However, the direct connection would create IF signals at DC, which is not suitable for measuring the phase noise.

To avoid this, an external wideband mixer and signal generator (E8257C) are inserted within the loop. In this measurement, a 10-GHz external signal is applied to the added mixer and the radar phase noise is measured at 5 GHz (1510 GHz). The measurement setup is pictured in Fig. 16(b). As shown in Fig. 16(c), the range correlation substantially improves the effective phase noise at IF (blue curve) compared to the original phase noise at the frequency synthesizer output (red curve). After subtracting the uncanceled phase noise from the canceled phase noise, the effective cancellation factor is plotted and compared with the theory (2 m) in Fig. 16(d). Very interestingly, the improvement factor of effective phase noise reaches a limit, which is set by the phase noise of the reference signal (DDFS + DAC) as illustrated in Fig. 16(c). The reason is as follows. The range correlation exploits the time-dependent correlation between the RX LO and returned signal. However, no such time-dependent correlation exists in the DAC quantization noise which is uncorrelated from sample to sample, thus it is not canceled by the range correlation for delays beyond one sample period. This behavior is clearly seen up to 100 kHz of offset frequencies. As the offset frequency increases, the cancellation factor decreases because of less correlation. As soon as the cancellation factor becomes less than the difference in noise power between the reference signal and synthesizer output, the effective phase noise at IF rises as well.

The above range correlation experiment implies two ways to improve the phase noise performance in the demonstrated radar architecture; one method is to increase the dynamic range of DAC so that the quantization noise of reference signal is lowered, and the other way is to operate the DAC at a higher sample rate so that the same quantization noise power is spread over wider bandwidth, lowering the noise power density.

VI. SNOW MEASUREMENT

A. Antenna Design

A quasi-optical antenna system based on a bistatic configuration provides a compact configuration while maintaining
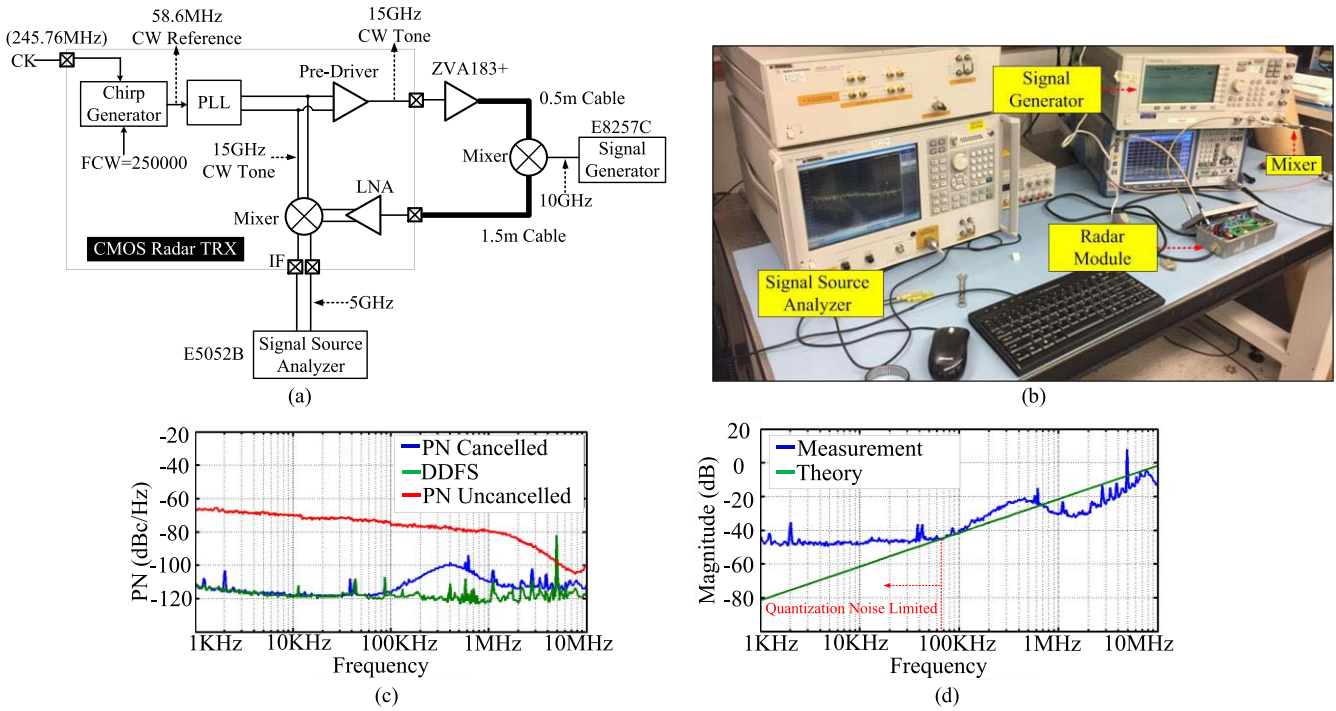
Fig. 16.   (a) Block diagram of range correlation measurement setup. (b) Measurement setup. (c) Measured phase noise after cancellation, DDFS reference phase noise, and un-canceled PLL phase noise. (d) Measured phase noise cancellation factor versus theory (2-m return).
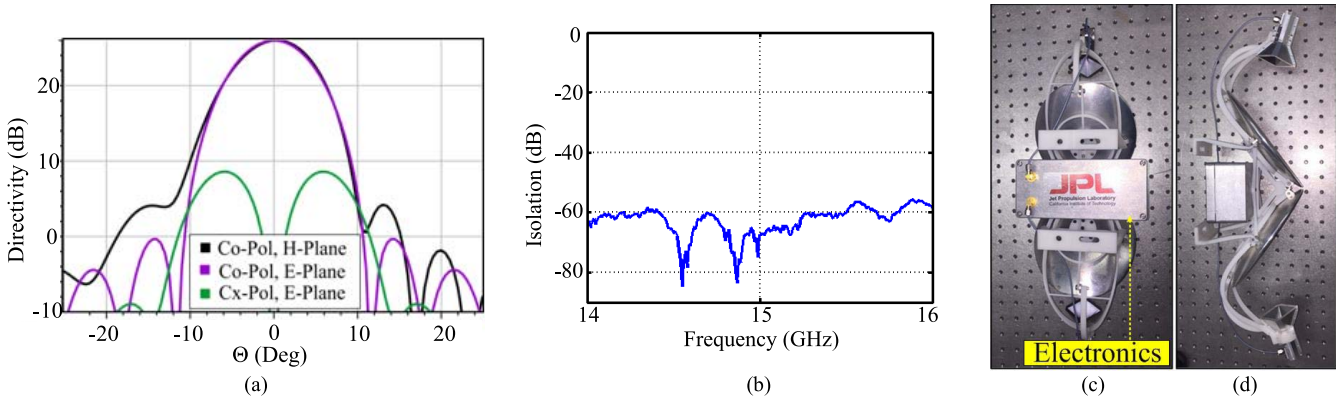

Fig. 17.   (a) Simulated radiation pattern of the offset-fed reflector system. (b) Measured TX to RX port isolation. (c) Backside view of radar module with antenna. (d) Top view of assembled radar module with antenna.

a high beam efficiency and high isolation between transmit and receive channels. The diameter of each transmit/receive reflector is 15 cm which keeps the system compact while preserving a reasonable spot size. The f-number is 0.8, which results in a compact quasi-optical system and a reasonable antenna feed size.

A diagonal horn has been chosen as the feed of this reflector for its beam performance and its compatibility with split block fabrication and assembly. The horn feed is designed to illuminate the reflector with a -10-dB edge taper has an aperture diameter of 1.8 cm and a length of 3.2 cm. The reflection coefficient is maintained at -20 dB in the 14–16-GHz frequency band. Its phase center is at 10.2 mm from its aperture. The feed is offset by 70° to avoid blockage with the main reflector beam. The quasi-optic system has been

designed using Gaussian beam propagation equations [19] and simulated using the commercial physical optics tools from GRASP [20]. The radiation pattern of the resulting beam from the reflector is shown in Fig. 17(a). The asymmetry in the main beam is caused by the offset configuration of the feed and reflector. Overall, it results in a beam of 26 dB of gain; at 5 m, it corresponds to a spot size diameter of 54 cm for a -3-dB edge field. The two halves of the bistatic system are tilted 3° to focus transmit and receive beams at 5 m, which is the nominal distance from the instrument to the top of the snow. Under this configuration, the TX-to-RX port isolation is measured using a vector network analyzer (VNA). The antennas' two SMA ports are connected to the VNA while the antennas are pointing at a K_u-band absorber, and a forward transmission (S21) is recorded as shown in Fig. 17(b). Within
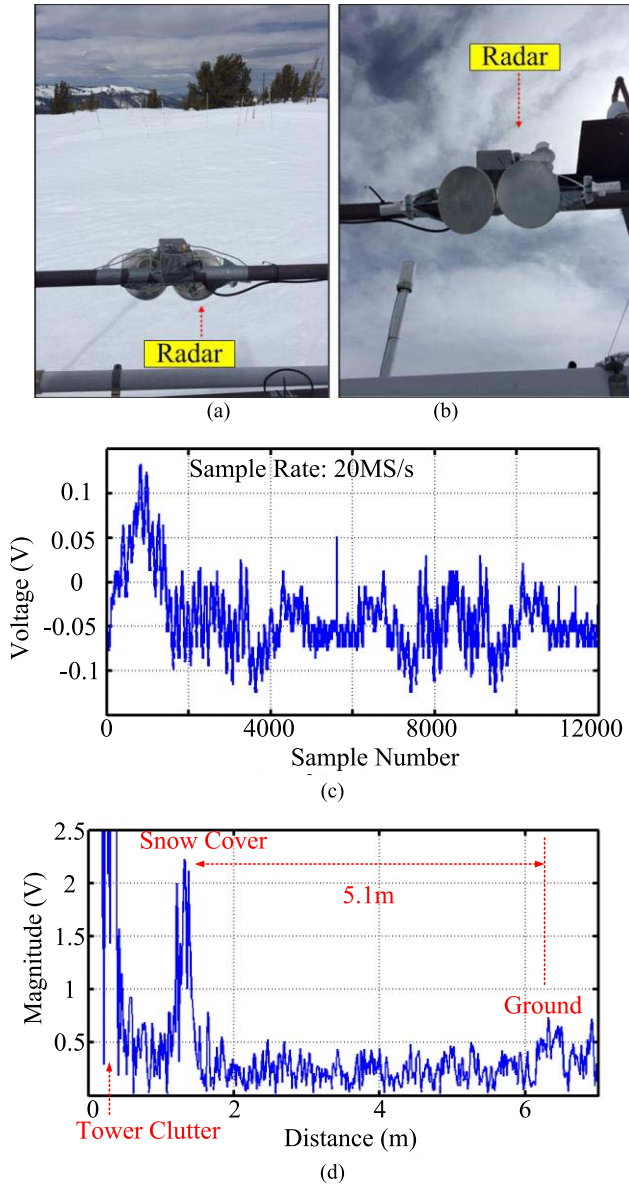
(a) (b)

(c)

(d)

Fig. 18. (a) Mammoth mountain deployment (backside view). (b) Mammoth mountain deployment (front view). (c) Sampled with 20 MS/s and recorded data in time domain. (d) FFT of recorded data.

the intended operating bandwidth (14–16 GHz), the designed antennas provide 60–80-dB isolation between the TX and RX, which is sufficient considering the target dynamic range of implemented radar system.

The final radar module with antenna is shown in Fig. 17(c) and (d). The instrument size is 51 cm × 20 cm × 20 cm, and the weight is 3.02 kg.

B. Snow Measurement at Mammoth Mountain

As a last step before launching in a UAV platform, the implemented radar was installed at the UCSB hydrology laboratory at Mammoth Mountain, CA, USA, on March 22, 2017. As shown in Fig. 18(a) and (b), the radar is mounted on the snow tower rail, and it points the snow surface with approximately 30° angle. The height of the rail, where the

TABLE IX
ULTRASONIC SNOW DEPTH MEASUREMENT PERFORMED
BY UCSB HYDROLOGY LABORATORY

Measurement Date	Measured Snow Depth in cm (Ultrasonic)
2017-03-22	506.55
2017-03-23	503.18
2017-03-24	510.89
2017-03-25	528.99
2017-03-26	525.79
2017-03-27	523.07
2017-03-28	519.50
2017-03-29	515.50
2017-03-30	507.99

radar is mounted, from the ground is 6.2 m. The radar recorded the depth of snow every 15 min for 7 days using the 20-MS/s Bitscope digitizer, and one of digitized and recorded time-domain data is shown in Fig. 18(c). A 2048 point windowed FFT is taken from the recorded data, resulting in a 4882-Hz per point (10 MHz/2048) resolution bandwidth in frequency domain. With the 0.098-MHz/m radar gain, a system gain in frequency domain is calculated as 0.0498-m per point (4882 Hz/0.098 MHz/m). Using this conversion, the measured snow depth is plotted in Fig. 18(d). As it can be seen, the snow cover is located at 1.2 m from the radar, and the ground is detected at 6.3 m. There also appears a strong frequency content at low IF, indicating cluttered reflections from the tower structure. Based on the retrieved data, the depth of snow is estimated at 5.1 m at the time of measurement. The measured amplitude difference between the ground and snow surface is approximately 12 dB. From Fig. 2(c), dry-snow's loss over 5.1 m is estimated to be 1–3 dB (2–6-dB round trip). Adding the ground scattering information (from -1 to -12 dB) from Table V makes the amplitude difference estimation in the range of 3–18 dB, which agrees with the measured data. In addition, according to the snow depth data measured by the existing ultrasonic instrument as shown in Table IX, the depth of snow varies over 5.03 and 5.28 m toward the end of March in 2017 [21], validating the radar measurements.

Building upon the initial field deployment, three major improvements can be made for the next snow season. First, because of relatively short distance measurement and possible dry snow conditions at the time of deployment, an external LNA was not included as part of the electronics, but as indicated by the signal strength in Fig. 18(c), higher front-end gain would have been more desirable to improve SNR (seen to be quantization noise limited). Second, the dynamic range of DAQ system needs to be improved allowing the full radar system dynamic range of 53 dB to be achieved. Third, better optical alignment is necessary to avoid bright returns from our test tower, which could potentially saturate the RX front end.

VII. CONCLUSION

A compact and low-power K_u-band CMOS radar transceiver has been implemented and demonstrated to measure

snow depth that is compatible with a low-altitude aircraft platform. The transceiver features a DDFS-DAC chirp generator to create the FMCW waveform and a ring-VCO-based PLL to convert it to the final K_u-band operating frequency. Employing a ring-VCO achieves the bandwidth and resolution required for snow sensing by avoiding large point counts associated with AWG generation of wideband radar waveforms, and the limited continuous bandwidth of LC-VCOs. The high phase noise characteristic of ring-VCOs is avoided by exploiting the range correlation effect where the use of the same LO in both transmit and receive paths creates a phase noise cancellation effect. The CMOS implementation allows the demonstrated radar to accommodate the payload of a small UAV platform. The demonstrated CMOS transceiver consumes 252.4 mW of power from a 1.1-V supply. The implemented radar system was deployed at Mammoth Mountain to perform real snow measurements and shows a good agreement with other snow depth measuring equipment.

REFERENCES

[1] *Sierra Nevada Conservancy*. Accessed: 2017. [Online]. Available: http://www.sierranevada.ca.gov

[2] *Review on Remote Sensing of the Snow Cover and on Methods of Mapping Snow*, World Metrological Organization, Geneva, Switzerland, 2004.

[3] J. Dozier, E. H. Bair, and R. E. Davis, "Estimating the spatial distribution of snow water equivalent in the world's mountains," *Wiley Interdiscipl. Rev., Water*, vol. 3, no. 3, pp. 461–474, 2016.

[4] J. Lee, Y.-A. Li, M.-H. Hung, and S.-J. Huang, "A fully-integrated 77-GHz FMCW radar transceiver in 65-nm CMOS technology," *IEEE J. Solid-State Circuits*, vol. 45, no. 12, pp. 2746–2756, Dec. 2010.

[5] T. Mitomo, N. Ono, H. Hoshino, Y. Yoshihara, O. Watanabe, and I. Seto, "A 77 GHz 90 nm CMOS transceiver for FMCW radar applications," *IEEE J. Solid-State Circuits*, vol. 45, no. 4, pp. 928–937, Apr. 2010.

[6] Y. Kim, A. Tang, K.-N. Liou, T. H. Painter, and M.-C. F. Chang, "A Ku-band CMOS FMCW radar transceiver with ring oscillator based waveform generation for snowpack remote sensing," in *IEEE MTT-S Int. Microw. Symp. Dig.*, Jun. 2017, pp. 64–66.

[7] M. C. Budge and M. P. Burt, "Range correlation effects in radars," in *Proc. IEEE Nat. Radar Conf.*, Apr. 1993, pp. 212–216.

[8] C. Matzler and U. Wegmuller, "Dielectric properties of freshwater ice at microwave frequencies," *J. Appl. Phys.*, vol. 20, no. 12, pp. 1623–1630, 1987.

[9] W. R. Tinga, W. A. G. Voss, and D. F. Blossey, "Generalized approach to multiphase dielectric mixture theory," *J. Appl. Phys.*, vol. 44, no. 9, pp. 3897–3902, 1973.

[10] J. W. Glen and P. G. Paren, "The electrical properties of snow and ice," *J. Glaciol.*, vol. 15, no. 73, pp. 15–38, 1975.

[11] M. T. Hallikainen, F. Ulaby, and M. Abdelrazik, "Dielectric properties of snow in the 3 to 37 GHz range," *IEEE Trans. Antennas Propag.*, vol. AP-34, no. 11, pp. 1329–1340, Nov. 1986.

[12] M. T. Hallikainen, F. T. Ulaby, and T. E. Van Deventer, "Extinction behavior of dry snow in the 18-to 90-GHz range," *IEEE Trans. Geosci. Remote Sens.*, vol. GRS-25, no. 6, pp. 737–745, Nov. 1987.

[13] F. T. Ulaby and M. C. Dobson, *Handbook of Radar Scattering Statistics for Terrain*. Norwood, MA, USA: Artech House, 1989.

[14] C. Elachi and J. V. Zyl, *Introduction to the Physics and Techniques of Remote Sensing*, 2nd ed. Hoboken, NJ, USA: Wiley, 2006.

[15] Y. Kim *et al.*, "An 8Gb/s/pin 4pJ/b/pin single-T-line dual (base+RF) band simultaneous bidirectional mobile memory I/O interface with inter-channel interference suppression," in *IEEE Int. Solid-State Circuits Conf. (ISSCC) Dig. Tech. Papers*, Feb. 2012, pp. 50–52.

[16] A. Tang, T. Reck, Y. Kim, G. Virbila, G. Chattopadhyay, and M.-C. F. Chang, "A 65 nm CMOS 88–105 GHz DDFS-based fractional synthesizer for high resolution planetary exploration spectroscopy," in *IEEE MTT-S Int. Microw. Symp. Dig.*, May 2016, pp. 1–3.

[17] S. D'Souza, F. Hsiao, A. Tang, S.-W. Tam, R. Berenguer, and M.-C. F. Chang, "A 10-Bit 2-GS/s DAC-DDFS-IQ-controller baseband enabling a self-healing 60-GHz radio-on-chip," *IEEE Trans. Circuits Syst. II, Exp. Briefs*, vol. 60, no. 8, pp. 457–461, Aug. 2013.

[18] Z. Xu, Q. J. Gu, Y.-C. Wu, H.-Y. Jian, and M.-C. F. Chang, "A 70–78-GHz integrated CMOS frequency synthesizer for *W*-band satellite communications," *IEEE Trans. Microw. Theory Techn.*, vol. 59, no. 12, pp. 3206–3218, Dec. 2011.

[19] P. Goldsmith, "*Quasioptical Systems: Gaussian Beam Quasioptical Propagation and Applications*," Piscataway, NJ, USA: IEEE Press, 1998.

[20] *GRASP 10.5.0 Simulation Software—TICRA*. Accessed: 2017. [Online]. Available: http://www.ticra.com

[21] *UCSB Snow Hydrology*. Accessed: 2017. [Online]. Available: http://www.snow.ucsb.edu

Yanghyo Kim (S'14–M'17–SM'17) received the Ph.D. degree from the University of California at Los Angeles, Los Angeles, CA, USA, in 2017.

He was with Keyssa Inc., from 2010 to 2013, where he commercialized the first 60-GHz CMOS contactless connector system. He is currently a Post-Doctoral Fellow with the Jet Propulsion Laboratory, Pasadena, CA, USA, where he has been involved in developing CMOS system-on-chip (radar, radiometer, and spectrometer) for space applications.

Theodore J. Reck (M'04–SM'15) received the B.S. degree in electrical engineering from The University of Texas at Austin, Austin, TX, USA, in 2000, and the Ph.D. degree in electrical engineering from the University of Virginia, Charlottesville, VA, USA, in 2010.

From 2010 to 2013, he was a NASA Post-Doctoral Fellow with the Jet Propulsion Laboratory (JPL), Pasadena, CA, USA, where he was involved in designing terahertz devices that utilize silicon micro-machining packaging. He is currently a Technical Staff Member with the JPL. His current research interests include RF-MEMS, terahertz metrology, and cryogenic monolithic microwave integrated circuit low-noise amplifiers.

Maria Alonso-delPino (S'10–M'14) received the degree in telecommunications engineering from the Technical University of Catalonia, Barcelona, Spain, in 2008, the M.S. degree in electrical engineering from the Illinois Institute of Technology, Chicago, IL, USA, in 2008, and the Ph.D. degree in signal theory and communications/electrical engineering from the Technical University of Catalonia, in 2013.

From 2014 to 2015, she was as a Post-Doctoral Researcher with the Technical University of Delft, Delft, The Netherlands. From 2015 to 2016, she was a NASA Post-Doctoral Fellow with the Jet Propulsion Laboratory (JPL), Pasadena, CA, USA, where she is currently a Researcher/Engineer with the Sub-Millimeter Wave Advanced Technology Group. Her current research interests include millimeter- and submillimeter-wave antennas, heterodyne and direct detection receiver technologies and measurement techniques.

Dr. Alonso-delPino was the co-recipient of the 2014 IEEE Terahertz Science and Technology Best Paper Award and a recipient of the Outstanding Reviewer Award of the IEEE TRANSACTIONS ON TERAHERTZ SCIENCE AND TECHNOLOGY in 2013.

Thomas H. Painter is currently a Principal Scientist and a Scientist V with the Jet Propulsion Laboratory (JPL), California Institute of Technology, Pasadena, CA, USA, and a Research Professor with the University of California, Los Angeles, CA, USA. He is also a Principal Investigator with the JPL Airborne Snow Observatory, where he focuses on integrated imaging spectrometer and LiDAR system to give the first-ever comprehensive, near real-time maps of snow water equivalent, and snow reflectivity in mountain basins. He has pioneered the understanding of the impacts of dust emission from land use change on snow and ice cover in mountain systems and the hydrologic response, and impacts of black carbon on regional glaciation in the Anthropocene. He has also developed cutting edge remote sensing and field models for snow properties from multispectral to imaging spectrometer sensors, scanning lidar systems, and radar systems. His efforts resulted in the development of the NASA Western Water Applications Office, JPL. His current research interests include snow hydrology, water resources applications from mountain snow and ice, radiative impacts of light-absorbing impurities on snow and glacier melt, and multisensor remote sensing of snow properties.

Dr. Painter was the President of the Cryosphere Focus Group, American Geophysical Union.

Hans-Peter Marshall received the B.S. degree in physics (with a minor in geophysics) from the University of Washington, Seattle, WA, USA, and the Ph.D. degree in civil engineering (with an emphasis in geotechnical engineering) from the University of Colorado at Boulder, Boulder, CO, USA.

He was with the Swiss Federal Institute for Snow and Avalanche Research, as a Visiting Ph.D. Student. He is currently an Associate Professor with the Department of Geosciences, and the Director of the Cryosphere Geophysics and Remote Sensing Group, Boise State University, Boise, ID, USA, and a Consultant for the U.S. Army Cold Regions Research and Engineering Laboratory, Hanover, NH, USA. He is also a Snow Scientist and a Glaciologist who uses geophysics and engineering tools to study the Cryosphere. His current research interests include spatial variability in snow and its effect on remote sensing, snow hydrology, and snow avalanches.

Dr. Marshall was a recipient of the 2010 AGU Cryosphere Focus Group's Young Investigator Award.

Edward H. Bair was with the University of California, the U.S. Army Corps of Engineers, Mammoth Mountain Ski Area, and has worked with a number of clients on a consulting basis. He is currently an Assistant Researcher with the Earth Research Institute, University of California, Santa Barbara, CA, USA. He uses remote sensing and field techniques to study the snowpack. He specializes in energy balance snowmelt modeling and avalanche formation in montane regions. His work spans a range of scales, from a few meters at the snowpit scale to thousands of square kilometers at the basin and mountain range scale. He has authored or co-authored over 40 journal papers on snow hydrology and snow avalanches.

Jeff Dozier (A'84–M'01–SM'03–LSM'15) received the Ph.D. degree from the University of Michigan, Ann Arbor, MI, USA.

From 1990 to 1992, he was the Senior Project Scientist with the NASA's Earth Observing System, when the configuration for the system was established. He is currently a Distinguished Professor with the Bren School of Environmental Science and Management, University of California at Santa Barbara, Santa Barbara, CA, USA, where he has taught since 1974. He founded the Bren School, where he served as the Dean for six years.

Dr. Dozier is a Fellow of the American Association for the Advancement of Science and the American Geophysical Union.

Goutam Chattopadhyay (S'93–M'99–SM'01–F'11) received the B.E. degree in electronics and telecommunication engineering from the Bengal Engineering College, Calcutta University, Calcutta, India, in 1987, the M.S. degree in electrical engineering from the University of Virginia, Charlottesville, VA, USA, in 1994, and the Ph.D. degree in electrical engineering from the California Institute of Technology, Pasadena, CA, USA, in 1999.

He is currently a Senior Research Scientist with NASA's Jet Propulsion Laboratory, and a Visiting Associate with the Division of Physics, Mathematics, and Astronomy, California Institute of Technology. From 1987 to 1992, he was a Design Engineer with the Tata Institute of Fundamental Research, Pune, India. His current research interests include microwave-, millimeter-, and submillimeter-wave heterodyne and direct detector receivers, frequency sources and mixers in the terahertz region, antennas, SIS mixer technology, direct detector bolometer instruments, InP HEMT amplifiers, mixers, and multipliers, high-frequency radars, and applications of nanotechnology at terahertz frequencies. He has authored or co-authored over 300 publications in international journals and conferences and holds more than 15 patents.

Dr. Chattopadhyay was a recipient of the Best Undergraduate Student Award from the University of Calcutta in 1987, the Jawaharlal Nehru Fellowship Award from the Government of India in 1992, and the IEEE MTT-S Graduate Fellowship Award in 1997, among various awards and honors. He was a recipient of the Best Journal Paper Award in 2013 by the IEEE TRANSACTIONS ON TERAHERTZ SCIENCE AND TECHNOLOGY, the IETE Prof. S. N. Mitra Memorial Award in 2014, the Best Antenna Application Paper Award of the European Conference on Antennas and Propagation in 2017, and the Distinguished Alumni Award from the Indian Institute of Engineering Science and Technology in 2017. He was also the recipient of more than 35 NASA Technical Achievement and New Technology Invention Awards. He is an Associate Editor of the IEEE TRANSACTIONS ON ANTENNAS AND PROPAGATION and an IEEE Distinguished Lecturer.

Kuo-Nan Liou received the B.S. degree from National Taiwan University, Taipei, Taiwan, and the Ph.D. degree from New York University, New York, NY, USA.

He is currently a Distinguished Professor of atmospheric sciences and the Director with the Joint Institute for Regional-Earth-System Science and Engineering, University of California at Los Angeles, Los Angeles, CA, USA. He has authored more than 260 peer-reviewed papers and 4 monographs on atmospheric radiation and cloud physics.

Dr. Liou was the recipient of the 1998 American Meteorological Society (AMS) Jule Charney Award, the 2010 COSPAR Biennial William Nordberg Medal, the 2012 IRC's Quadrennial Gold Medal, and the 2013 American Geophysical Union (AGU) Roger Revelle Medal, the highest honor in atmospheric sciences from AGU. He was bestowed the 2018 highest AMS Award Carl-Gustaf Rossby Research Medal "for intellectual leadership and seminal contributions to improving the theory and application of atmospheric radiative transfer and its interactions with clouds and aerosols," as well as being elected as a Foreign Member of the Chinese Academy of Sciences in 2017. He was elected to the National Academy of Engineering in 1999 and the Academia Sinica in 2004.

Mau-Chung Frank Chang (S'76–M'79–SM'94–F'96–LF'17) is currently the President of the National Chiao Tung University, Hsinchu, Taiwan. He is also the Wintek Chair Professor of electrical engineering with the University of California, Los Angeles, CA, USA. His current research interests include the development of high-speed semiconductor devices and high-frequency integrated circuits for radio, radar, and imaging system-on-chip applications up to terahertz frequency regime.

Dr. Chang is a member of the U.S. National Academy of Engineering, a Fellow of the U.S. National Academy of Inventors, and an Academician of the Academia Sinica of Taiwan. He was a recipient of the IEEE David Sarnoff Award in 2006 for developing and commercializing GaAs HBT and BiFET power amplifiers for modern high-efficiency and high-linearity smart phones throughout the past 2.5 decades.

Adrian Tang (GS'11–M'12–SM'15) has been with Jet Propulsion Laboratory (JPL), Pasadena, CA, USA, since 2013, where he was the first to demonstrate sub-centimeter accurate mm-wave imaging radar in silicon technology with demonstrations at 144 and 155 GHz, the first to demonstrate predistortion in CMOS mm-wave transmitters above 150 GHz, and the first to demonstrate CMOS-based passive radiometers with enough sensitivity to support passive imaging. He is currently with the JPL, where he leads the development of a wide range of CMOS system-on-chip chipsets for planetary, earth science, and astrophysics space instruments.